11-18-2020

Examination of Early Stage Grey Iron Solidification through the Development of Fast-Quench Methodology

James C. Liggett
Georgia Southern University

Recommended Citation

Liggett, James C., "Examination of Early Stage Grey Iron Solidification through the Development of Fast-Quench Methodology" (2020). *Honors College Theses*. 539.
https://digitalcommons.georgiasouthern.edu/honors-theses/539

Examination of Early Stage Grey Iron Solidification through the Development of Fast-Quench Methodology

An Honors Thesis submitted in partial fulfillment of the requirements for Honors in

Allen E. Paulsen College of Engineering and Information Technology: Department of Mechanical Engineering

By

J. Chandler Liggett

Under the mentorship of Dr. Mingzhi Xu and Dr. Jingjing Qing

ABSTRACT

As grey iron casting accounts for a significant share of the foundry industry, proper understanding of the effects of solidification and growth mechanisms on the mechanical properties of grey iron is crucial. Prior experimentation has been performed examining early stage solidification and growth of the carbon phase of ductile iron, in which rapid quench samples are obtained which detail austenite-graphite interactions during solidification. This prior experimentation is built upon in though this research and applied to examine the early stage growth of flake graphite in grey iron. The purpose of this research is to validate a proposed fast-quench method by observing type A flake graphite development and producing cooling curves for both quenched and unquenched grey iron samples. It was found that proper inoculation can allow for type A flake graphite morphologies in the proposed thin section sample castings. Cooling curves were additionally obtained for both quenched and unquenched samples, however the rate of cooling was slower than predicted in simulation and samples were quenched directly from the liquid state rather than during solidification which allowed for analysis of type E graphite rather than the desired type A morphology. This research successfully set the stage for future work in developing more accurate cooling curve simulations and obtaining precise fast quench samples for metallography at various stages in the solidification and growth of grey iron.

Thesis Mentor:________________________

Dr. Mingzhi Xu and Dr. Jingjing Qing

Honors Director:_______________________

Dr. Steven Engel

November 2020

Department of Mechanical Engineering

University Honors Program

Georgia Southern University

Acknowledgements:

The support and encouragement of Dr. Mingzhi Xu and Dr. Jingjing Qing are gratefully acknowledged. The mentorship of Dr. Mingzhi Xu and the help and expertise lent by Dr. Jingjing Qing based on prior research in this field were invaluable. Additionally, the support provided by Carolina Metalcasting in facilitating the sample collection is gratefully acknowledged and appreciated. The assistance of Shelton Fowler and Sam Holt during the sample collection process is also gratefully acknowledged. Lastly, facilities and equipment provided by the Georgia Southern University Department of Mechanical Engineering were greatly influential to the success of this project.

1. Introduction:

1.1 Introduction to Grey Iron and its Importance to the Foundry Industry

The production and casting of grey iron is of critical importance within the foundry industry. According to the World Foundry Organization, in 2018 grey iron accounted for over 30% of the United States market share. [1] Not only does grey iron account for 30% of all castings produced, but more grey iron is cast in the USA than any other alloy. Grey Iron leads by 29% over ductile iron which is the second most produced alloy by tonnage. [1] For this reason, the casting of grey iron and other iron alloys has received much attention in recent years as efforts are made to better understand the factors determining the mechanical properties and overall performance of the alloy.

1.2 Cast Iron Microstructure and Its Relation to Mechanical Properties

Currently, the majority of research performed on cast iron has been focused on graphite nucleation sites. Although typically the iron matrix phase is considered to have the largest influence on mechanical properties, it is actually the carbon phase in the form of graphite which has the largest effect on cast iron mechanical properties. This is due to the ability of graphite to either facilitate or hinder crack propagation. [2]

Thus, it is the graphite morphology rather than the iron matrix which differentiates the two most common cast iron alloys. Ductile iron is a cast iron featuring nodular graphite morphology which is ideal for inhibiting crack propagation. Ductile iron features high ductility coupled with respectable strength due to the nodular graphite morphology. [3] Grey iron, on the other hand, features a sharper, more angular graphite morphology which leads to the occurrence of stress concentrations at the angular graphite surfaces. These stress concentrations make the material more brittle than ductile iron in thick castings. [3]

Grey iron does however possess superior machinability, thermal conductivity, and damping properties which make it a popular choice in many engineering applications. [3] Additionally, the material is more attractive from a casting standpoint because commercial grey iron chemistry features a carbon equivalent just below eutectic composition (4.3 wt% carbon equivalent (CE) as shown in Eq. 1). This near-eutectic composition facilitates the lowest melting temperature and the least shrinkage of all ferrous materials which makes it an extremely easy-to-cast alloy. [4] [5] An example of the difference between ductile iron nodular graphite and grey iron flake graphite morphologies is shown in Figure 1 and Figure 2 respectively. [6]

$$CE = C(wt\% + \frac{1}{3}Si(wt\%) \qquad (1$$

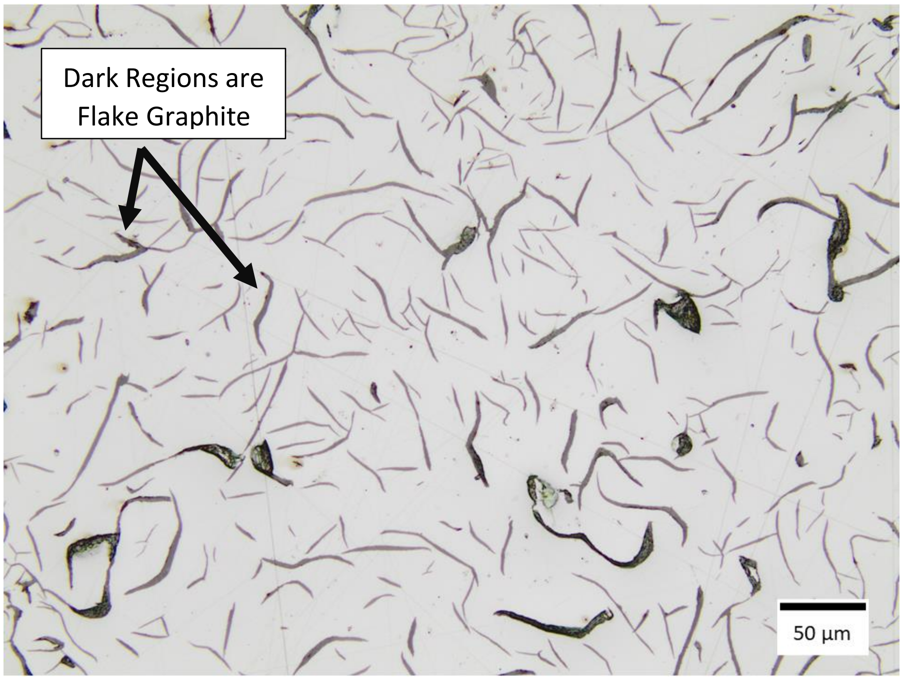

Figure 1: Grey Iron Flake Graphite Morphology

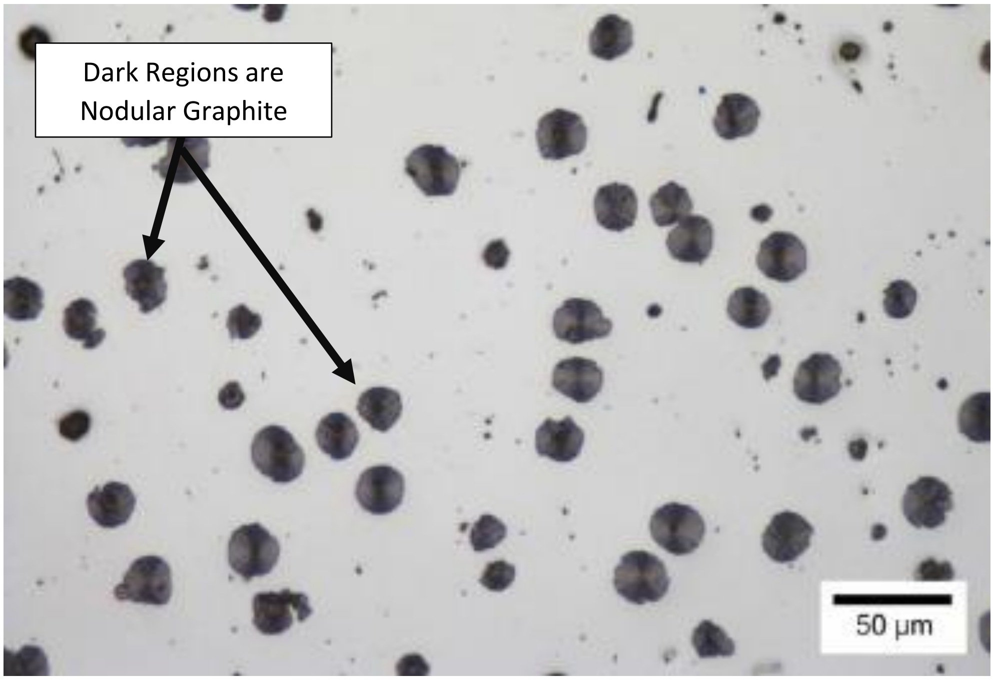

Figure 2: Ductile Iron Nodular Graphite Morphology
Reproduced/Adapted from [6] *with permission from Springer Nature*

1.3 Graphite Nucleation in Cast Irons

As graphite morphology wields such a prominent influence on material behavior, it is important to fully understand the factors which influence the resulting morphology. Nucleation, the process by which heterogenous nuclei are formed to provide favorable sites for graphite particle growth, is of great importance in controlling graphite morphology and has been extensively studied. Effective heterogeneous nucleation requires particles which are solid, with low lattice disregistery with graphite, and are finely dispersed within the melt prior to graphite precipitation. [7] For this reason, it has been established that the austenite phase solidification is ineffective for graphite nucleation. [8] As Riposan et al remarked, residual graphite would be an ideal location for further graphite nucleation as it would offer the lowest lattice disregistry, but heterogeneous nucleation on other substrates is possible depending on certain conditions. [7]

It was found that sulfide micro-inclusions offer the possibility for such heterogeneous nucleation sites. (MnX)S, where X is an additional element such as Fe, O, Si, Al, Zr, Ti, Ca, or Sr, has been shown to serve as an effective nucleation site for flake graphite because these complex sulfides have low crystallographic misfit with graphite. [7] [9]

Sulfide compounds serve as effective sites for graphite nucleation for three primary reasons. First, sulfides already exist as solids in solution with liquid iron because their melting temperatures are appreciably higher than that of iron. [10] Additionally, the enthalpy of formation for such compounds is negative, which is necessary for the formation of such compounds to be spontaneous. For a sulfide to be a truly ideal nucleation site it would additionally have a low crystallographic misfit with graphite. [10] As determined by Riposan et al., unaltered MnS compounds in un-inoculated iron features a simple morphology, and the misfit between graphite and MnS is large. [7] However, when inoculant elements such as calcium, zirconium, or aluminum are added to the melt, complex (Mn,X)S sulfides are then formed which feature a much lower misfit with graphite. [10] This is explained by a three-stage model of graphite nucleation in which i) small micro-inclusions are formed in the melt by deoxidizing elements, ii) complex (Mn,X)S compounds nucleate at the micro-inclusions, and iii) graphite nucleates on the (Mn,X)S sides with the lowest crystallographic misfit. [7] A depiction of the three-stage model is shown in Figure 3, reproduced with permission from research performed by Riposan et al.[11] This three-stage nucleation method is supported in work by González, Espita, and Sierra. [10]

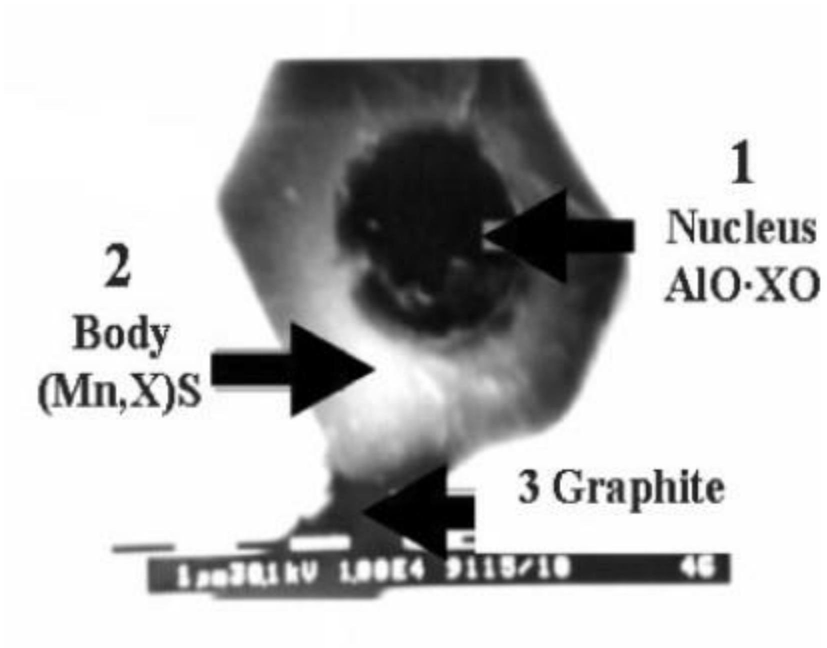

Figure 3: Three-stage Nucleation Model for Flake Graphite Growth
Reproduced/Adapted from [11] with permission from Taylor and Francis Online [12]

Graphite nucleation is additionally related to austenite growth through the influence of austenite on these (Mn,X)S compounds. It is proposed that optimum graphite growth, defined as uniformly distributed type A graphite growth, takes place in conditions coupled with finely spaced, multi-junctioned primary austenite dendrites. [13] The reason for this is proposed by Strande et al. As austenite growth proceeds, microconstituents which are not dissolvable in austenite are rejected from the dendrite arms into the interdentritic melt, providing a localized high concentration of compounds suitable for graphite nucleation. [13] It is therefore proposed that alloying elements which refine the austenite dendrite formation, such as Al, Ti, or V, will also affect the number of graphite nucleation zones, increasing the eutectic cell count. [13]

1.4 Graphite Growth Mechanisms and their Importance in Cast Irons

Although extensive study exists regarding nucleation sites of graphite, comparatively little research has been performed studying graphite growth mechanisms after nucleation. Additionally, although nodular and flake graphite both nucleate on similar or identical nucleation sites, their final structure and the impact which they have on the material properties of the iron could not be more dissimilar. [8] For these reasons, the factors effecting the shape and size of the graphite must take place during growth after initial nucleation. It has been theorized that differences between flake and spheroidal graphite occur due to change in preferred growth directions, and thus does not depend on nucleation sites nearly as much as on the overall growth mechanism. [14]

Work has been performed by Qing, J. et al to develop a model for spheroidal graphite growth mechanisms in Ductile Iron. It was found that spherical graphite growth occurred in two phases, i) curved graphene layers formed circumferentially around a nodule surface and ii) graphene layers formed circumferentially within conical substructures. [6] It was found that the basal plane distortion in graphite growth occurred primarily due to disregistry between the growing graphene layers and the initial nucleation site. Circumferential growth of graphite has been accepted as the natural growth direction of graphite in liquid iron, and in the first growth phase this circumferential growth mechanism is allowed to continue unhindered. [14] [6] Additionally, circumferential growth would often stem from multiple nucleation sites on a single nucleus, thus multiple growth fronts have been observed to advance simultaneously. These growth fronts would eventually meet and merge, accommodated by crystallographic defects. [6] Additionally, the curvature of graphene layers is high when the nodule diameter is small and thus crystallographic defects must occur to accommodate the high curvature. [6] As the growth fronts continued to meet, and the diameter of the nodule became larger, the disregistry would increase between the growth fronts, causing gaps to occur. These gaps then lead to the transition from circumferential growth to circumferential growth within conical substructures. [6]

As it has been established that spheroidal graphite is the naturally occurring graphite phase, Grey iron must then be produced by modifying the graphite morphology to form flake graphite. [15] When impurities are present in solution with liquid iron, such as [S] or [O_2], the surface tension of the liquid is reduced. This reduced surface tension causes the spherical morphology to branch out and deteriorate into lamellar flake-like structures. [15] This may seem contrary to established practices, as it is commonly known that in practice spheroidal graphite does not occur naturally without alloy additions such as Mg or Ce present in the melt. However, these alloy additions primarily function as scavengers of impurities which would reduce surface tension. [15] [16]

Following nucleation, austenite and flake graphite solidification then occurs in the form of a eutectic cell which is spheroidal in nature but consists of austenite and interconnected flake graphite plates. [17] These eutectic cells will continue to grow, branching out to form the flake graphite morphology of Grey Iron. [17] The cooling rate of the material upon solidification will then play a primary role in influencing the growth and characteristics of these eutectic cells, both influencing the number and size of eutectic cells and the branching of the graphite phase within the cell. [17] [18] The size and number of eutectic cells formed within the sample will largely influence the final microstructure of the grey cast iron.

1.5 3-Dimensional Growth Structures of Grey Iron

3D analysis of grey iron microstructures has supports the eutectic cell growth hypothesis of grey iron, with 3D Grey Iron flakes being observed to be arranged in large eutectic cells [19]. These clusters being centered around an initial nucleation site and branching out in graphite flakes [20]. As each eutectic cell can be reduced to an initial nucleation event, the number of eutectic cells within a given sample can be used as a measurement of inoculation efficiency [20].

1.6 Research Scope and Measurable Outcomes

In this research, early stage solidification of grey iron and the growth of flake graphite eutectic cells will be examined through development of an experimental method by which early stage growth microstructures may be obtained. This will be accomplished by further development of an experimental method by which early grey iron quench specimens from a variety of chemistries may be obtained. These early quench specimens will be used to obtain eutectic cell microstructures during various solidification and growth stages allowing for study of austenite-graphite interactions. Work performed previously on early stage nodular graphite growth by Dr. Jingjing Qing will be applied here to grey iron samples by modifying the fast quench methodology used in that experiment for use in grey iron casting.

This research aims to develop and validate a means by which the early-stage growth interactions between austenite and graphite may be studied. Furthermore, this research aims to obtain early-stage solidification microstructures of grey cast iron for examination. Specific desired outcomes in this research used to quantify fulfillment of the research goals include the following. First, it should be determined whether the mold apparatus used in ductile iron experimentation will allow for adequate flake graphite nucleation and growth in samples with grey iron chemistry. The fast cooling rate of the mold apparatus could result in high undercooling which produces type B graphite rosettes rather than the desirable finely dispersed type A graphite. Second, cooling curves for the grey iron samples in the mold apparatus must be obtained to facilitate accurate quench timing for the capture of various solidification stages. Simulation work will be done beforehand using metal casting simulation software, and the final results will be compared for accuracy. Lastly, early stage graphite grow microstructures will be obtained for growth mechanism study. These early stage microstructures obtained from fast quench experimentation will represent "snapshots" in the solidification process allowing for a better understanding of austenite-graphite interactions. These desired outcomes to be obtained in this research will be used to lay the groundwork for further early stage flake graphite growth research.

2. Experimental Methods

2.1 Mold Design for Grey Iron Casting and Rapid Quench

To achieve the proposed experimental goals, an experimental procedure was adopted which allowed for fast-quenched cast grey iron samples to be obtained. The primary concern in developing a fast quench experiment for grey iron samples involves the selection of an appropriate mold material which can withstand the high temperatures involved in ferrous casting while allowing for fast heat transfer rates. Fused Quartz tubing features a high softening point well above the liquidus temperature of most iron alloys and was selected for this experiment. The high strength at low wall thickness of this material allows for the selection of a very thin mold wall thickness. Minimal wall thickness resulting in fast quench responses by reducing the thermal barrier between the iron and the quench medium. For these reasons, fused quartz tubing was chosen as the ideal mold material for this experiment.

Rapid quench rates were thus facilitated by selection of a quartz tubular mold with a 10mm inner diameter and a wall thickness of 1mm. The selected mold design is shown below in Figure 4. The mold assembly consists of an outer quartz shell for the collection of cast samples with an inner quartz-shielded thermocouple assembly for temperature measurement. Using glass blowing techniques, the 10mm quartz tube was cut to length and fused together at one end. An inlet was then created in the mold wall halfway along the length of the tube to allow metal to flow into the mold. A vent was created about above this to allow gas to escape. The target size for the inlet and vent was around 6mm in diameter.

In order to obtain a cooling curve for this experiment, a thermocouple assembly was designed for the interior of the mold. A K-type thermocouple was selected for the purpose of this experiment as it has a maximum operating temperature just above the liquidus temperature of typical Grey Iron and is frequently used in solidification analysis for iron alloys. [21] [22] To construct the thermocouple assembly, the thermocouple wires were inserted through a small double-bore alumina tube which isolated both thermocouple wires from contact with each other down the length of the mold. The wires were then twisted and welded together at one end and crimped into a thermocouple connected on the other. A smaller quartz tube just larger than the outer diameter of the alumina rod was then cut and fused in a similar manner to the outer quartz shell. The alumina rod and was slid inside of this protective sleeve to eliminate direct contact between the thermocouple leads and the liquid metal. Care was taken that the welded tip of the thermocouple was in direct contact with the quartz sleeve to allow for fast response of the temperature readings. This complete thermocouple assembly was lastly inserted into the 10mm tube and cemented in place using a ceramic investment casting slurry, making sure to keep the thermocouple assembly concentric to the mold.

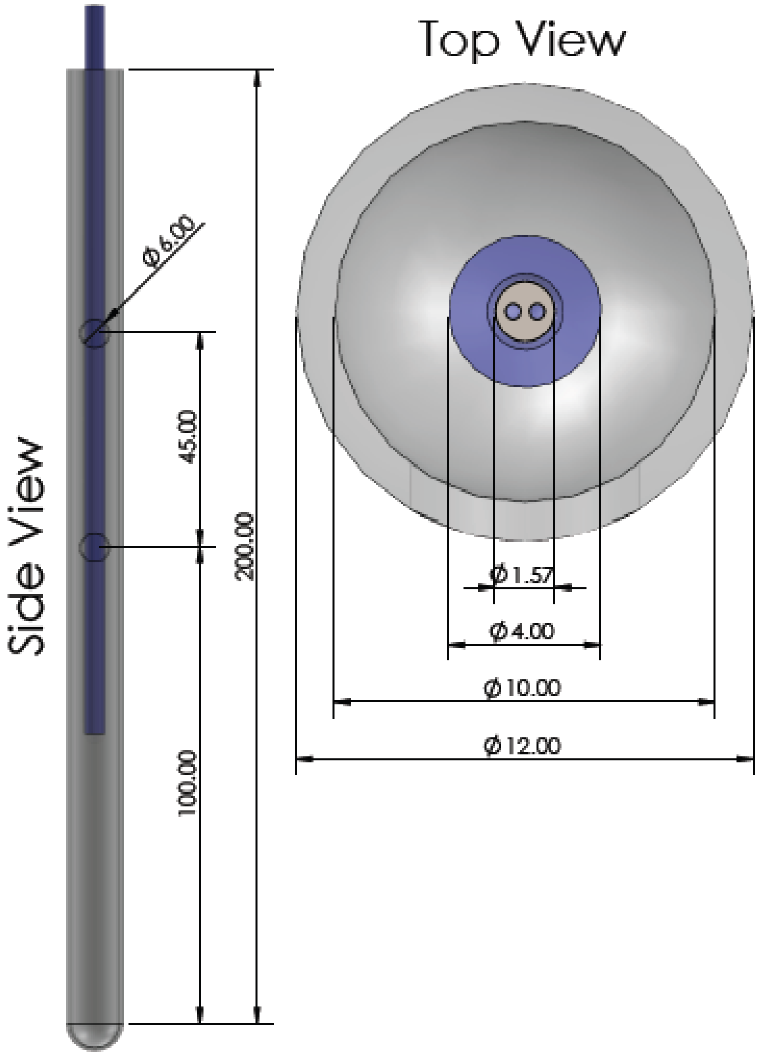

Figure 4: Sample Fast-Quench Quartz Mold Design (Units in mm)

After the mold assembly was constructed, it was affixed to a 1m steel rod for handling during the experiment. The rod was held temporarily in place by adhesive while layers of ceramic investment casting slurry and silica sand were built up around it, firmly securing the mold assembly to the handling rod. Each layer was allowed to dry before the next was applied. After the ceramic coating was sufficiently thick, the assembly was prepared for use by attaching a 3m thermocouple extension wire to the thermocouple connector and then wrapping the thermocouple components in kaowool for protection. The final thermocouple equipped mold assemblies are shown in Figure 5. This process was repeated to produce four separate thermocouple sample molds. Three additional molds were prepared with no thermocouples to collect intermediate samples without cooling curves.

Figure 5: Quartz Mold Assemblies for Fast-Quench Grey Iron Samples

2.2 MAGMA Simulation

Before the physical sample collection, a simulation was performed using MAGMA metal casting simulation software. Class 30 Grey Cast Iron alloy parameters were selected for an investment casting simulation to predict the solidification behavior in a thin quartz mold as closely as possible. It was assumed that no thermal barrier existed between the mold wall and molten metal, so a high heat transfer coefficient of 3500 W/m^{2}K was selected between the casting and the mold wall. Figure 6 shows the mold geometry used for the simulation, with the translucent material representing the mold shell and the solid grey material representing the cast sample.

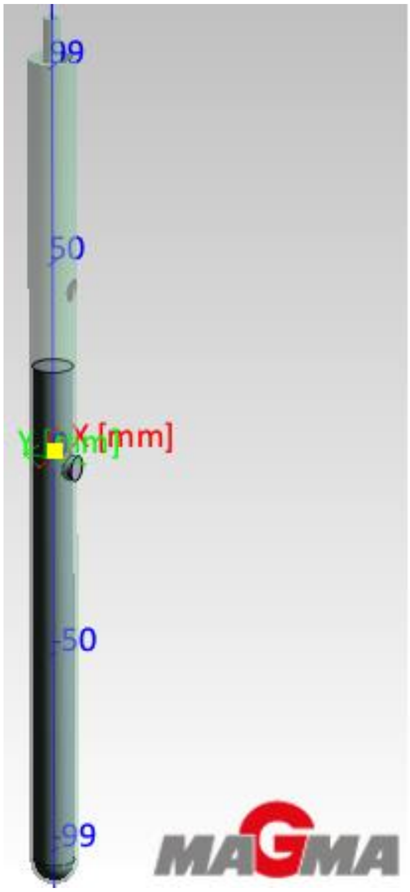

Figure 6: MAGMA Metal Casting Simulation Geometry for Solidification Study

2.3 Sample Collection

The fast-quench experiment was performed with the support of Carolina Metal Casting, using samples obtained from their production line. Samples were obtained directly from the ladle immediately after tapping out by immersion of the tubular mold into the liquid at a depth just above the inlet but below the vent. Quenched samples were then quickly immersed in a water bath at room temperature. Each sample was provided with its own separate water bath to avoid quench temperature variations from sample to sample. The samples without thermocouple assemblies were collected first. The target holding times identified by the MAGMA simulation were 5, 10, and 15 seconds. During the holding period the samples were inserted into a kaowool lined crucible initially at room temperature to maintain steady cooling.

The sample molds with thermocouple assemblies were examined next. The thermocouple assemblies were connected to a computer and temperature recording was started. Two molds were filled and immediately quenched in water at room temperature. The remaining two molds were collected as unquenched samples by placing them in the kaowool insulated environment until fully solidified. The collected thermocouple data was then extracted and used to construct cooling curves for the quenched and unquenched sample conditions.

2.4 Metallography

The samples obtained were then prepared for microstructure examination by cutting along their cross sections for mounting and polishing. The samples were each cut by a low speed diamond saw near the tip of the sample into a 10mm segment. The end of the segment closest to the tip of the sample was selected for examination in order to study the location of fastest quench response. The samples were then mounted in bakelite specimen holders for ease of polishing. The polishing process was performed on an auto-polisher in 180, 600, 800, and 1200 grit sandpaper stages in 1 minute polishing increments followed by a 3 μm and 0.1 μm diamond polish for 3 minutes each. Specimens were then examined with an optical microscope at 100x, 200x, 500x, and 1000x magnification. Metallographic images were taken of the quenched samples unetched, but the unquenched sample was examined further by etching with a 2% nital solution.

3. Data

3.1 Cooling Curve Simulation Data

From the MAGMA simulation, simulated cooling curve data was obtained which approximates the predicted experimental cooling rate of the sample and is shown in Figure 7. The liquidus and solidus temperatures were identified for Class 30 Grey Iron, and times were selected which represent critical locations for solidification study. As shown in Figure 7, critical locations on the cooling curve during solidification include the thermal arrest region in which the rapid cooling is halted by the release of latent heat during solidification. According to MAGMA simulation, quench times between 5 and 15 seconds would capture early stage solidification for examination. Thus, it was determined that one immediate quench sample would be obtained, three delayed quench samples would be obtained after holding periods of 5, 10, and 15 seconds in a kaowool insulated environment, and one unquench sample would be collected. In this manner behavior across the entire solidification process could be examined. During the experiment, actual quench times were recorded, and actual holding times were measured to be 6, 8, and 14 seconds between mold filling and the water quench.

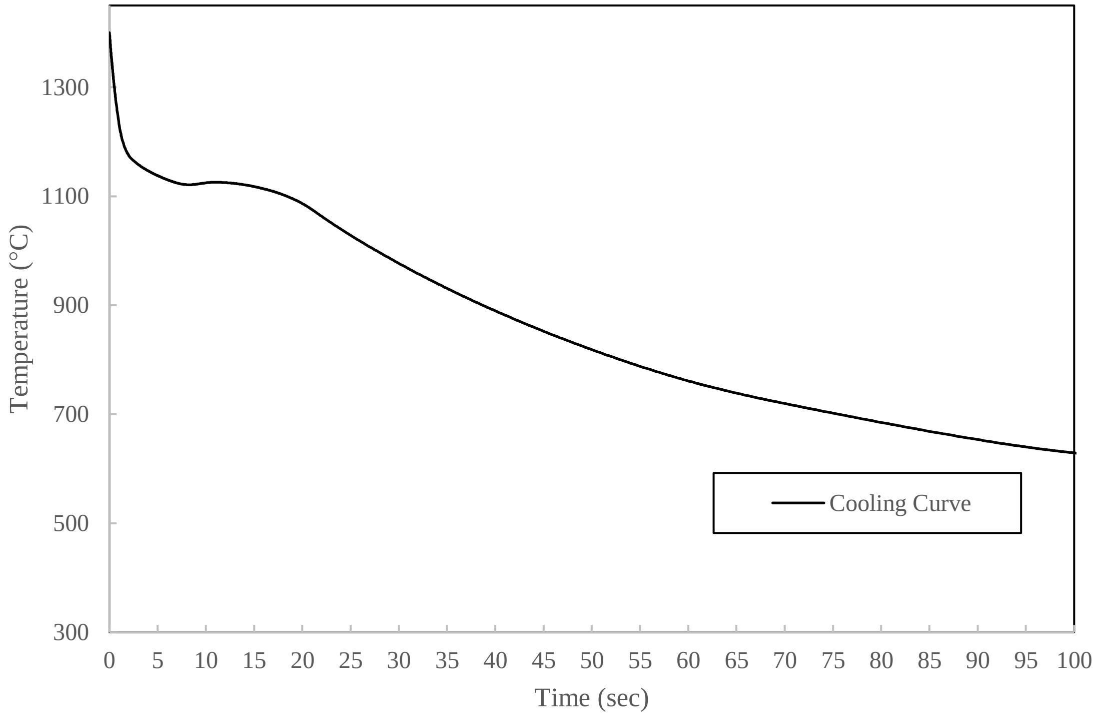

Figure 7: Class 30 Grey Iron Cooling Curve Obtained from MAGMA Simulation Data.

3.2 Chemistry and Thermal Properties

Environmental and chemical variables were measured prior to and during the experiment for use in interpreting results. The Grey Iron chemistry was measured prior to sample collection and is shown in Table 1. The recorded ladle temperature during the experiment averaged to 1340 °C.

Table 1. Grey Iron Sample Chemistry

	C	Si	Cr	Cu	Mg	Mn	P	S
wt%	3.4	2.15	0.249	0.0493	<0.001	0.736	0.0271	0.0152

An equilibrium solidification step diagram for grey iron of the chemistry specified in Table 1 was developed using JMatPro material property analysis software and is presented in Figure 8. This diagram allows for the theoretical phase constituents of the samples to be determined at different temperatures during the equilibrium cooling process.

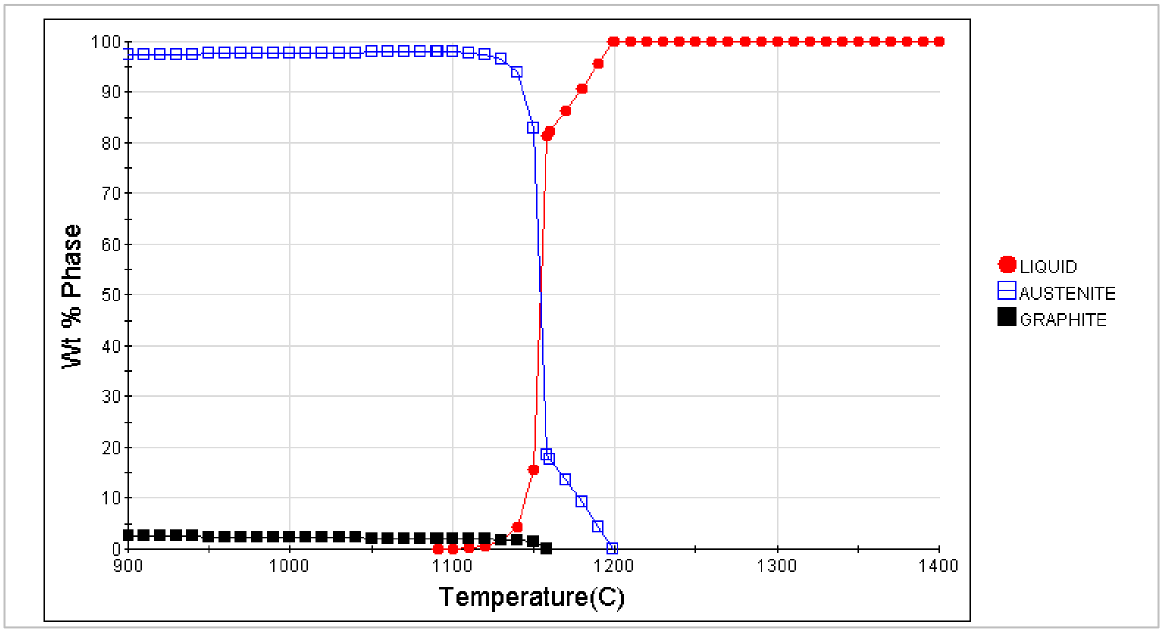

Figure 8: JMatPro Equilibrium Solidification Step Diagram for Selected Grey Iron Chemistry

Experimental cooling curves were obtained during sample collection from the temperature readings recorded by the thermocouples. The cooling curves for the unquenched sample and the immediate quench sample recorded during the experiment are shown overlayed in Figure 9.

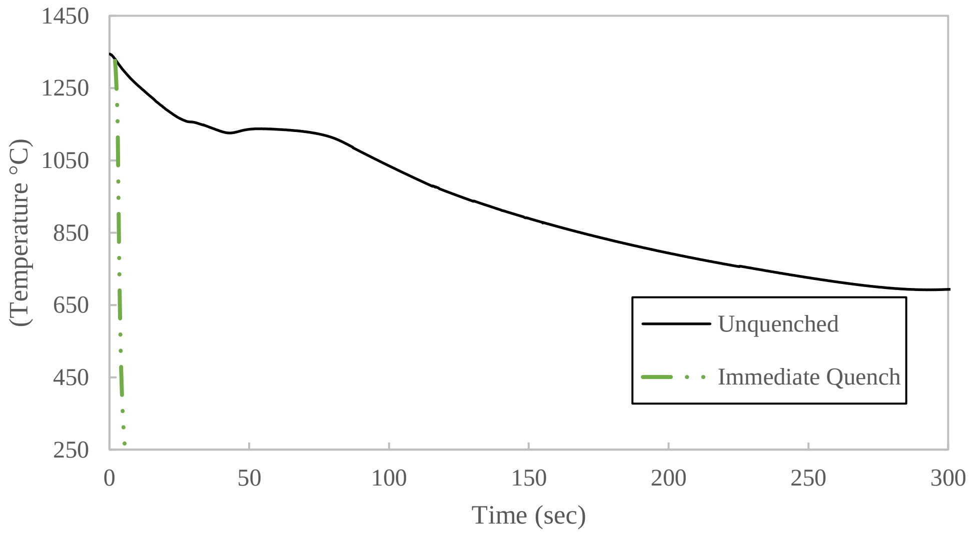

Figure 9: Experimental Grey Iron Cooling Curves Obtained for Unquenched and Immediate Quenched Samples

3.3 Metallography

Metallographic images were obtained of each sample using an optical microscope and are presented here for reference. The unquenched sample microstructure is first presented in Figure 10. Figure 10.a shows the unetched unquenched grey iron microstructure. Figure 10.b shows the same microstructure after etching with a 2% nital solution. Figure 11 shows the unetched unquenched grey iron sample at low magnification for observation of the morphology and distribution of flake graphite through the sample. Figure 12 displays a side-by-side comparison of representative flake graphite structures found through the unquenched sample.

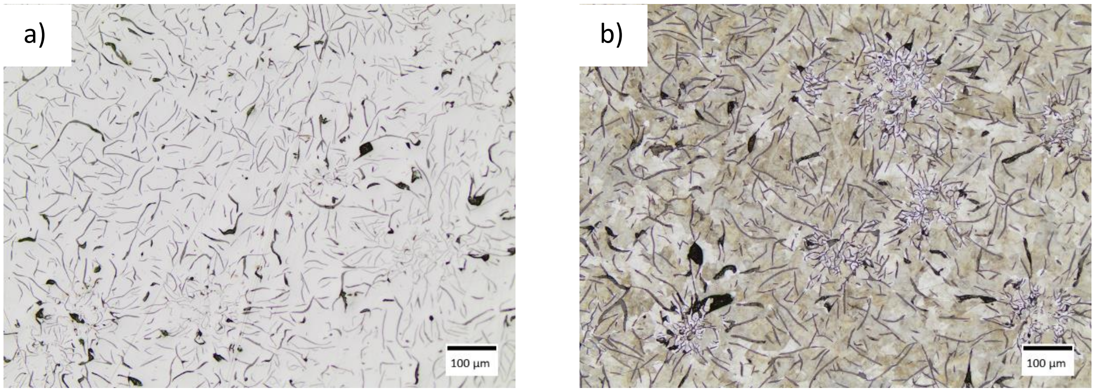

Figure 10: Unetched (a.) and Etched (b.) Microstructure of the Unquenched Grey Iron

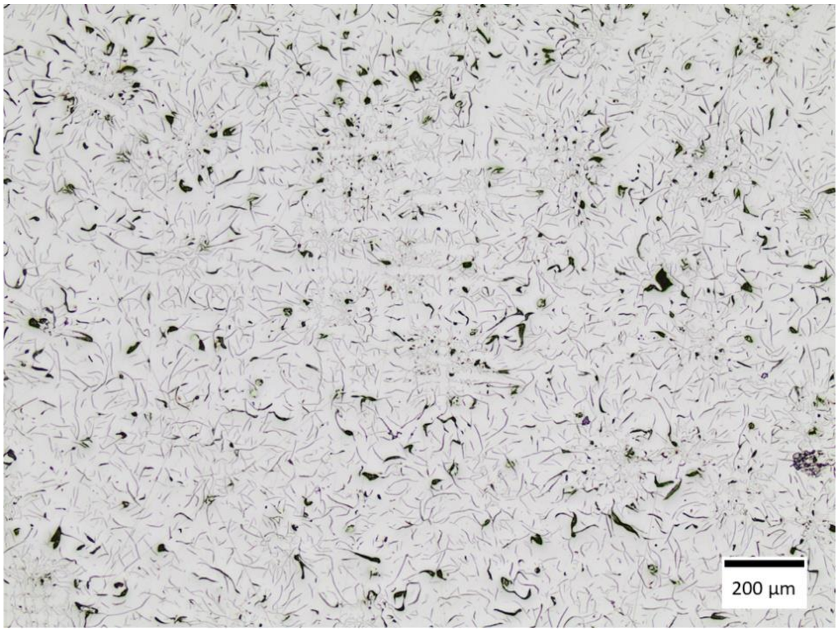

Figure 11: Microstructure of Unquenched Unetched Grey Iron at Low Magnification

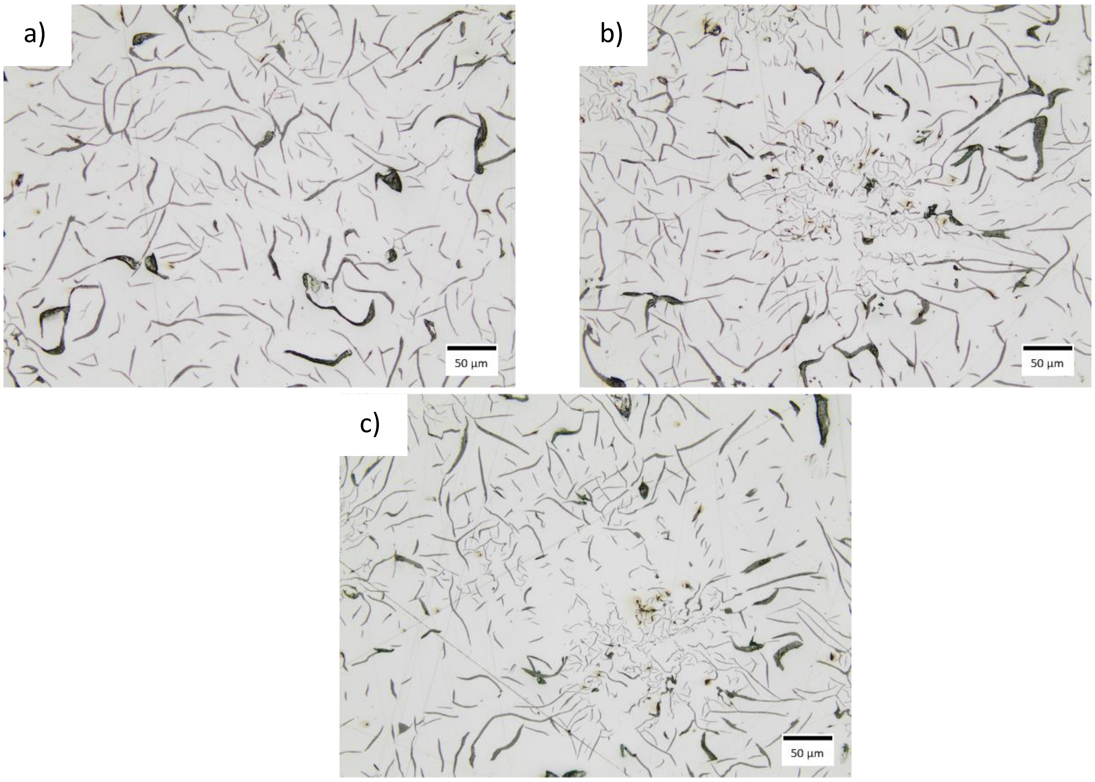

Figure 12: Flake Graphite Morphology Comparison of the Unquenched Grey Iron Sample

The microstructures obtained for the quench samples are shown in Figures 13, 14, and 15. The microstructures resulting from the immediate quench process are shown in Figure 13, 14, and 15 a), while the samples held for 6, 8, and 14 seconds prior to the quench process are shown in b), c), and d) of the same figures respectively. Microstructure images are unetched and shown in increasing magnifications from Figure 13 to Figure 15.

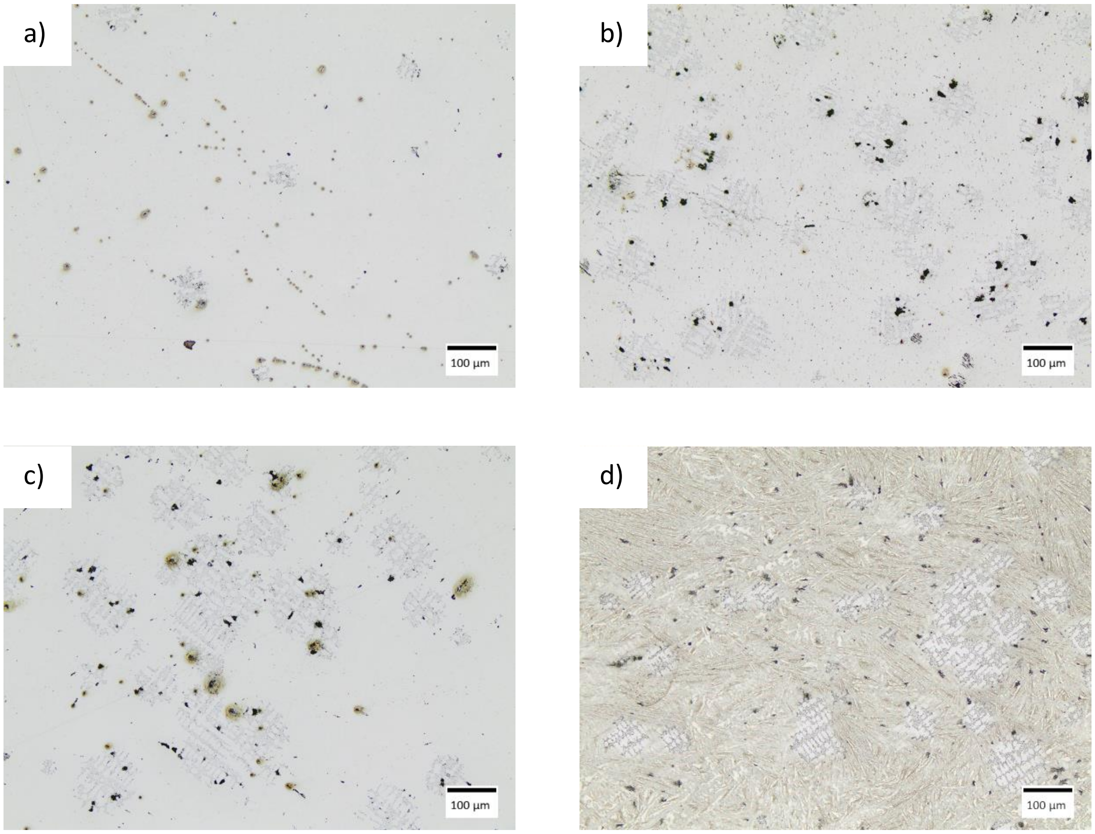

Figure 13: Immediate Quench (a.) and 6, 8, and 14 Second Delayed Quench (b., c., and d. respectively) with Microstructures at 100 μm Scale

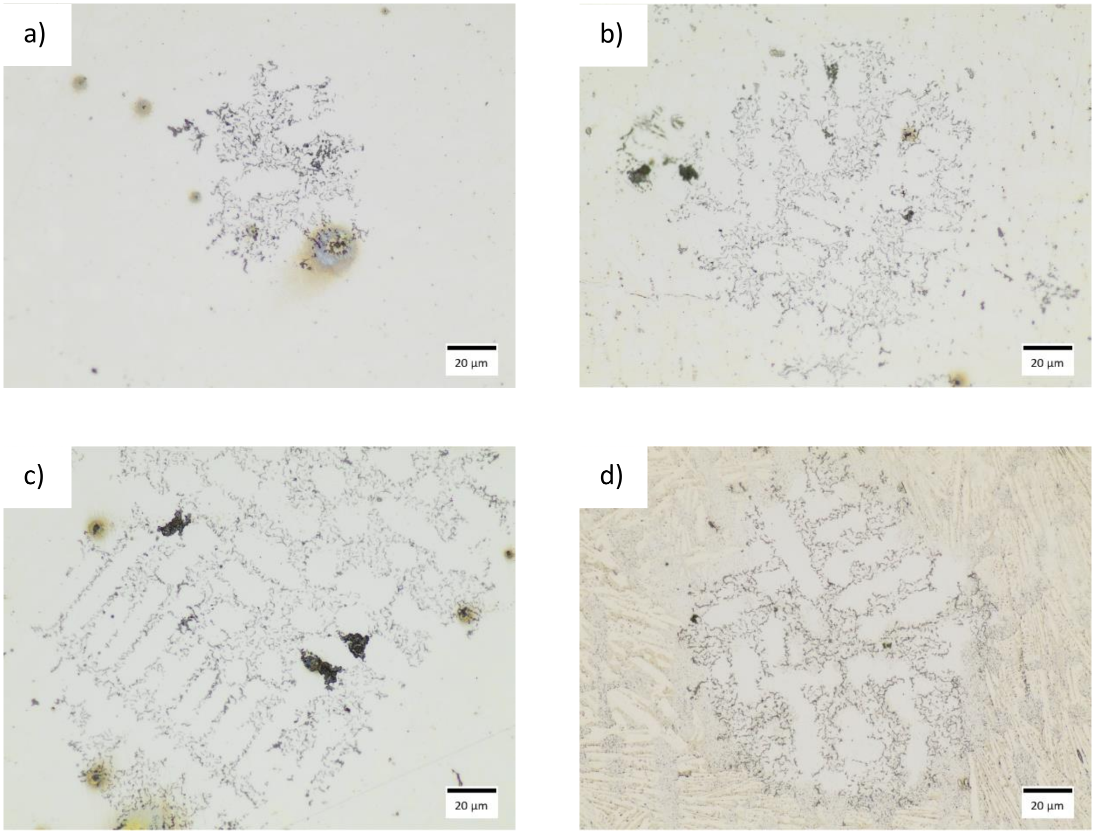

Figure 14: Immediate Quench (a.) and 6, 8, and 14 Second Delayed Quench (b., c., and d. respectively) with Microstructures at 20 µm Scale

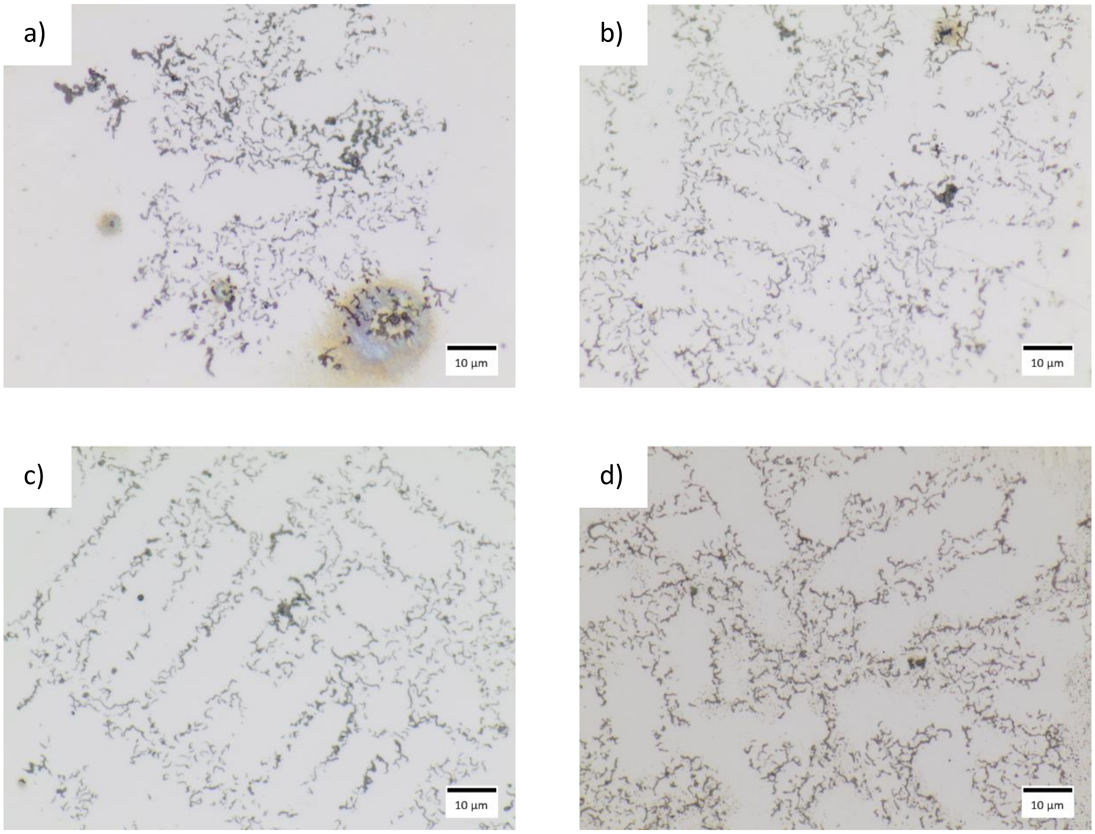

Figure 15: Immediate Quench (a.) and 6, 8, and 14 Second Delayed Quench (b., c., and d. respectively) with Microstructures at 10 µm Scale

4. Results

4.1 Results from Chemistry Analysis

From the sample chemistry collected, the carbon equivalent of the iron can be computed. Using Eq. 1 of section 1.2 in this paper, the carbon equivalent was found to be 4.12 wt%. This corresponds to a slightly hypoeutectic grey iron composition as the eutectic composition of cast iron is 4.3 wt% CE. [23] A sample calculation for the carbon equivalent is shown below. Because the grey iron is of hypoeutectic chemistry, austenite can be expected to be the primary phase during solidification from liquid. Primary austenite however only accounts for a small percentage of the final microstructure since the iron chemistry is so close to eutectic composition.

$$CE = C + \frac{1}{3}Si = 3.4\ wt\% + \frac{1}{3}2.15\ wt\% = 4.12\ wt\%$$

4.2 Results from Cooling Curve Analysis

Cooling curve analysis furthermore allows critical transformation temperatures to be identified, including the liquidus temperature, the eutectic transformation start temperature, and the solidus temperature. To process the cooling curve and better identify critical points, the first derivative of the cooling curve was computed. In first derivative cooling curve analysis, extremes in the derivative curve correlate to critical points in the cooling curve. This is because the rate of cooling (i.e. the first derivative of the cooling curve) changes noticeably at phase transformation locations due to latent heat of fusion. [24] Figure 16 shows the plot of the first derivative of the cooling curve against the actual cooling curve. The first derivative plot was exponentially smoothed to reduce noise and allow for easier identification of critical points. Peaks and troughs were identified which correlated with the Liquidus, Eutectic Transformation Start (ETS), and Solidus points in the curve. The times at which the critical points occurred in the first derivate curve were identified and the corresponding temperature on the cooling curve was obtained. From this data, the liquidus, ETS, and solidus temperatures were identified and are shown in Table 2.

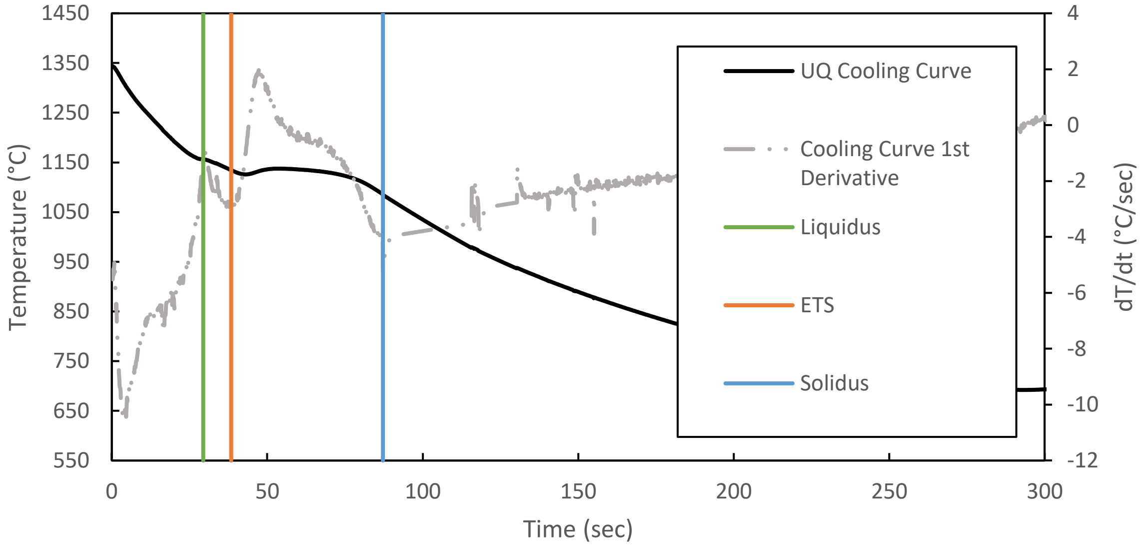

Figure 16: First Derivative Analysis of the Grey Iron Cooling Curve

Table 2. Critical Cooling Curve Points from First Derivative Analysis

	Temperature (°C)	Time (sec)
Liquidus	1156	29.4
ETS	1132	38.4
Solidus	1085	87.2

The unquenched and quenched sample cooling curves were used to extrapolate cooling curves for the delay quench samples. This was performed by adding an offset to the immediate quench cooling curve equal to the holding time applied to each sample prior to quench. Each sample was additionally assumed to begin the quench process at the temperature specified on the unquenched cooling curve at the time of quench. These were plotted against the unquenched cooling curve and are shown relative to the three critical cooling curve points in Figure 17. This allows predictions to be made regarding the phases present in the grey iron samples. Data can also be extrapolated from unquenched cooling curve to determine the approximate temperature upon quench for each sample. This can be accomplished by approximating the temperature of the quenched samples after each holding period to be equivalent to the temperature of the unquenched sample at the same time during solidification. This information is shown in Table 3.

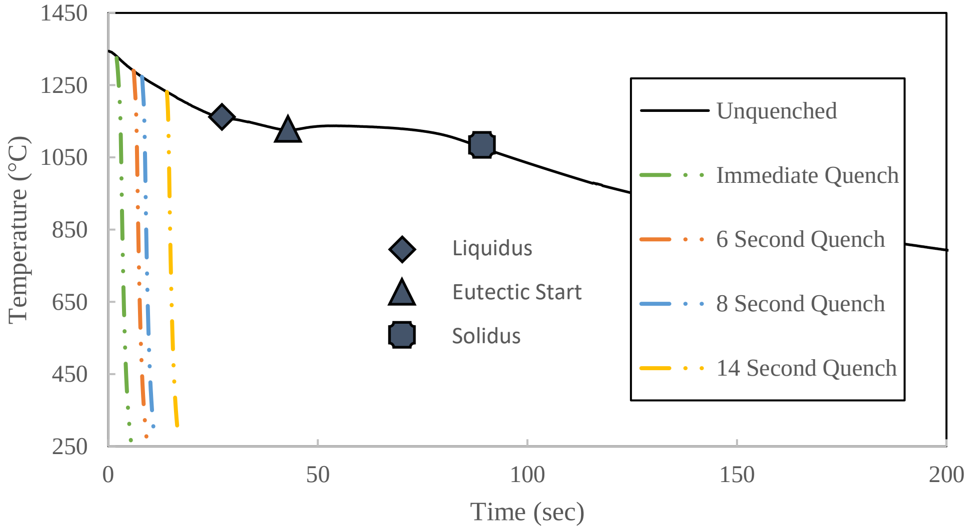

Figure 17: Extrapolated Delayed Quench Cooling Curves Shown Relative to Critical Cooling Points

Table 3. Extrapolated Quenched Sample Starting Temperature

Quench Delay	Quench Start Temperature (°C)
Immediate Quench	1340
6 sec	1290
8 sec	1273
14 sec	1231

4.3 Metallography

From the metallographic images gathered from the unquenched sample, it was found that type A, B, and E graphite were present in the sample. Figure 11 shows a low magnification overview of the general flake graphite distribution throughout the sample, from which it can be observed that Type A graphite morphology primarily dominates the structure. Figure 12 shows higher magnification images of the various graphite structures observed in Figure 11. Type A graphite morphology can be seen in Figure 12.a. In Figure 12.b, instances of Type B graphite can be seen in more detail. Graphite rosette formations can also be seen in the etched unquenched sample in Figure 10.b. Figure 12.c shows in more detail instances of type E graphite formations, in which the flake graphite is organized in more dendritic patterns.

5. Discussion

5.1 Experimental Method and Process

Overall, the process and methods followed in this research resulted in successfully obtaining unquenched and fast quench results. The thin tubular quartz molds allowed for extremely fast quench response with little observable insulation due to the mold shell. Additionally, the thermocouple data obtained was able to accurately chart the cooling behavior of the cast iron samples for further study. Like the mold wall, the quartz sleeve selected to protect the thermocouple did not appear to appreciably delay the cooling curve reading from the actual cast iron temperature. The design was successful in obtaining cast samples with accompanying cooling curves.

It was noticed however that the inlet diameter of the quartz mold restricted the material flow into the mold which resulted in noticeable difficulty during mold filling. Additionally, the vent created in the mold was too close to the inlet, making it difficult for consistently keeping it above the liquid for adequate gas dispersion. Despite these challenges, quality samples were collected for microstructure analysis.

5.2 Unquenched metallography and microstructure

From the experimental results, several important findings were discovered relating to future development of this research. The first of which being that grey iron samples cast in the thin tubular molds were able to form predominantly type A graphite upon solidification. Initially it had been questioned whether type A graphite would be able to form in the thin cross section mold due to fast cooling rates. If the degree of undercooling is too great, type B graphite would primarily result. [23] As seen in Figure 11 however, finely dispersed type A graphite was primarily obtained in the unquenched sample.

Type A graphite is the result of growth and solidification of eutectic cells at low undercooling. For this reason, rapid solidification tends to negatively affect the amount of Type A graphite which forms due to high amounts of undercooling. [23] Good inoculation however aids in Type A graphite formation at faster cooling rates as a multiplicity of favorable nucleation sites allows graphite nucleation to be more thermodynamically favorable. This requires less undercooling to for the flake graphite to solidify, which thus favors type A graphite growth over type B.

The prevalence of type A graphite in the unquenched sample as seen in Figure 11 therefore indicates good inoculation in the melt prior to the pour which allowed for many favorable nucleation sites. This multiplicity of favorable nucleation sites allowed for graphite nucleation at lower undercooling which helped the eutectic cell to nucleate and grow to the desired Type A graphite even at rapid cooling. As discussed in the introduction, Manganese Sulfides in the form of (Mn,X)S provide favorable carbon nucleation sites. From the sample chemistry provided in Table 1 it can be seen that the sample contained substantial amounts of each which would promote the formation of type A flake graphite.

According to established practices, the desired stoichiometric relationship between S and Mn for the purpose of graphite nucleation is given in Eq. 2. [23] Additional Mn is sometimes desired in excess of the S content for a few reasons, primarily to ensure that detrimental FeS sufides do not form, but also to serve as an alloying element. According to Equation 2 and the sample S content from Table 1, only 0.026 wt% Mn is strictly needed for complete MnS formation as shown in the sample calculation; however an excess of Mn will ensure that all S is tied up in MnS sulfides. In this sample, an excess of 0.71 wt% Mn is predicted to remain after all S is tied up as predicted in the stoichiometric ratio in Eq. 2. The remaining Mn will serve as an alloy addition for solid solution strengthening, although excessively high Mn tends to reduce tensile strength and hardness for a softer grey iron. [23] Suggested limits for excess Mn content range from 0.3 wt% to 0.5 wt%. [23]

$$\%S \times 1.7 = \%Mn \qquad \text{Eq. 2}$$

$$0.0152\ wt\%\ S \times 1.7 = 0.026\ wt\%\ Mn$$

5.3 Quenched Sample Metallography and Microstructure

From the unquenched sample cooling curve and extrapolated quenched sample cooling curves shown in Figure 17, it is immediately apparent that the samples were quenched prior to primary austenite nucleation. As shown in Table 2, in a kaowool insulated environment initially at room temperature it takes 29.4 seconds for the 10mm diameter sample to cool to the liquidus temperature. The longest holding time prior to quench in this experiment was 14 seconds, significantly under the time required to reach the liquidus temperature. Metallographic examination also confirms that the samples were quenched directly from the liquid phase prior to either primary austenite nucleation or type A graphite nucleation. From Figures 13, 14, and 15, only type D flake graphite morphology is present, featuring finely distributed interdendritic flake graphite formed into distinct eutectic cell formations. Type D graphite occurs at very high undercooling such as that experienced in an immediate quench scenario when grey iron is rapidly cooled from the liquid phase. [23]

Because the samples were in each case quenched directly from liquid, examination of austenite-graphite growth interactions during normal solidification was not possible. In this case, the effect of liquid superheat on the development of highly undercooled eutectic cells can be observed, with later quench times resulting in larger, more developed eutectic cell regions as observed at various magnifications in Figures 13, 14, and 15. Figure 13 shows the overall eutectic cell size and distribution differences between immediate quench and delayed quench samples, with the immediate quench sample shown in 13.a showing smaller less developed eutectic cells and 13.d showing the largest most developed eutectic cells. Because in each case the samples were quenched directly from liquid, the observed size difference between samples was not due to the capture of various growth stages but rather due to differences in liquid temperatures at quench, with the immediate quench sample being quenched at the highest temperature and the 14 second delay sample being quenched at the lowest temperature as seen in Figure 17 and Table 3.

Cooling rate has a large part to play in the determination of phases resulting from various solidification conditions. The development of flake graphite during solidification requires carbon diffusion from austenite to regions of higher carbon concentration. At extremely fast cooling rates, carbon diffusion is limited as it is a time and temperature dependent process. [25] [15] Cooling rate is driven thermodynamically by the difference in temperature between mediums. In the case of this experiment, heat transfer is accomplished by a combination of conduction and convection between the sample, the quartz mold, the quench medium, and potential vapor films which may occur as water is vaporized during the quench. In both convection and conduction, larger temperature differences result in faster rates of heat transfer. For this reason, higher initial liquid temperatures will drive much higher heat transfer rates and push the material below the solidus temperature faster than for samples which were quenched later in the cooling process. Table 3 shows the decrease in quench starting temperatures for the quench samples. When this information is compared to the metallographic images obtained for quenched eutectic cell size in Figures 13, 14, and 15, a correlation can be made which supports the hypothesis that higher liquid quench temperatures result in smaller less developed eutectic cell formations consisting of type D graphite.

5.4 Comparison between Simulated and Experimental Cooling Curve Results

There is observed to be significant disparity between the MAGMA cooling curve simulation and the actual experimental behavior which led to the selection of quench holding periods which were inadequate to allow the metal to begin solidification at the time of quench. According to MAGMA simulation results, quench holding times of 5, 10, and

15 seconds should have provided examples of graphite morphology as primary austenite formed and type A graphite nucleated and grew from the melt. However, because the actual cooling of the samples occurred at a much slower rate all samples were obtained directly from liquid.

There are a few different factors which could account for this disparity between simulated cooling results and experimental data. First, it could be that the overall heat transfer rate between the environment and the sample was significantly lower for the quartz tubular mold compared to the 1mm thick simulated ceramic investment shell which was selected to approximate the molding condition. However, due to the nature of such a thin walled shell, it is unlikely that the difference in conduction rates between the two mediums would render significantly different results such as those found in experimentation. The second more likely cause for the disparity between the two cooling curves is that the kaowool insulated environment was not considered during the MAGMA simulation process. The default environmental conditions were retained for this simulation, which would be standard convection between the mold and an environment at room temperature. The Kaowool insulated environment used in the experiment would retain heat transferred to the surrounding air which would slow the overall rate of heat transfer as the air temperature increased. This insulated environment used in the experiment would thus significantly slow the experimental cooling process compared to the MAGMA simulated results from an uninsulated air-cooled environment.

As actual experimentally determined cooling behavior has been obtained for this experimental setup, in the future more appropriate quench holding times may be selected to better capture various early-stage solidification microstructures. However, this experimental data will only necessarily hold true for cast iron samples of the same chemistry. If the effects of varying alloying element additions on solidification are to be obtained, or if a hypereutectic cast iron is to be studied, it would be of immense advantage to obtain a means of simulation which would more accurately predict the experimental cooling curve.

5.5 Future Work

This research accomplished many preliminary research outcomes for future research to be performed. Through this experiment, an experimental cooling curve was obtained for the selected grey iron chemistry and initial validation of the experimental method and setup were performed. It was also verified that type A graphite could successfully be obtained from a small diameter quartz tubular mold. Furthermore, fast quench response was obtained and measured from a water quench performed on the same samples. For these reasons it was validated that early stage growth and solidification microstructures of type A graphite may be obtained through this experiment.

To further develop this research, more simulation work with be performed using MAGMA metal casting simulation software to develop solidification heat transfer parameters which closer match the experimental conditions. The effect of conduction parameters through the sample mold will be investigated to determine the degree to which general approximated mold material selections affect the accuracy of heat transfer calculations for the quartz mold material. Work will also be done to determine how best to incorporate the kaowool insulated environment in the MAGMA simulation.

Further work to be done in this research also includes using the cooling curve obtained to select more appropriate quench holding periods which allow for early nucleation and growth of graphite prior to quench. Since the actual experimental cooling behavior of the selected cast iron chemistry is known, holding times may be selected which accurately produce early stage microstructures in primary phase growth as well as eutectic cell growth. When coupled with more accurate simulation data, this research can be extended to both hypoeutectic and hypereutectic cast iron chemistry.

Lastly, improvements may be made in the mold design to address the mold filling difficulties encountered. It was found that the mold inlet should be larger to allow for easier entry of liquid metal into the mold. Additionally, the air vent should be further from the inlet to prevent it from passing under the liquid level. It is proposed that in the future a combination of glass blowing techniques and diamond abrasion be used to increase the size of the inlet hole by a factor of 1.5 while also moving the location lower along the tube. The combination of a longer thermocouple assembly and an inlet closer to the sample tip would both allow for more accurate temperature readings at the location of fastest quench response and allow for the vent to be positioned further away from the metal inlet.

6. Conclusion

This research validated a proposed fast-quench method for obtaining early stage solidification microstructures of grey cast iron. The purpose of this research was to obtain early stage microstructures in order to study the interactions between flake graphite and austenite during early grain growth after nucleation. It was found that a small diameter, thin shelled quartz tubular mold with an internal thermocouple assembly was able to successfully obtain early stage microstructures of cast grey iron samples through fast quench treatments. Cooling rate simulations were performed using MAGMA metal casting simulation software which ultimately did not match experimentally determine cooling curve information and led to the samples being quenched prior to the occurrence of nucleation and solidification in the sample. For this reason, early stage solidification microstructures were not ultimately obtained. However, valuable results were discovered which validated the experimental methodology for further study. It was found that type A graphite successfully formed in unquenched samples collected in the thin section molds, ensuring future study will be able to observe the development of type A graphite rather than the less desirable type B graphite. Additionally, both quenched and unquenched cooling curves for the samples were obtained for future use, and process improvements were developed to enhance the success of future experiments.

References:

[1] 2018, *WFO Global Foundry Report 2018*.

[2] Ghassemali, E., Hernando, J. C., Stefanescu, D. M., Dioszegi, A., Jarfors, A. E. W., Dluhoš, J., and Petrenec, M., 2018, “Revisiting the Graphite Nodule in Ductile Iron,” Scr. Mater., **161**(2019), pp. 66–69.

[3] Askeland, Donald R.; Wright, W. J., 2016, *The Science and Engineering of Materials*, Cengage Learning, Boston, MA.

[4] Stadtler, W. A., ed., *Metals Handbook: Forging and Casting*, American Society for Metals.

[5] Razaq, A., Yin, Y., Zhou, J., Shen, X., Ji, X., and Ullah, I., 2019, “Influence of Alloying Elements Sn and Ti on the Microstructure and Mechanical Properties of Gray Cast Iron,” Procedia Manuf., **37**(2019), pp. 353–359.

[6] Qing, J., Richards, V. L., and Van Aken, D. C., 2016, “Examination of Spheroidal Graphite Growth and Austenite Solidification in Ductile Iron,” Metall. Mater. Trans. A, **47**(12), pp. 6197–6213.

[7] Riposan, I., Chisamera, M., Stan, S., and White, D., 2009, “Complex (Mn , X) S Compounds - Major Sites for Graphite Nucleation in Grey Cast Iron,” China Foundry, **6**(4), pp. 3–8.

[8] Campbell, J., 2015, *Complete Casting Handbook: Metal Casting Processes, Metallurgy, Techniques and Design: Second Edition*, Waltham, MA.

[9] Moumeni, E., Stefanescu, D. M., Tiedje, N. S., Larrañaga, P., and Hattel, J. H., 2013, “Investigation on the Effect of Sulfur and Titanium on the Microstructure of Investigation on the Effect of Sulfur and Titanium on the Microstructure of Lamellar Graphite Iron,” Metall. Mater. Trans. A, **44A**(November), pp. 5134–5146.

[10] González, H. M., Espitia, P. P., and Sierra, R. A., 2017, “Fading and Graphite Nucleation Sites in Grey Iron Inoculated Using Silicon Carbide,” Rev. Matéria, **22**(2).

[11] Riposan, I., Chisamera, M., Stan, S., Hartung, C., and White, D., 2010, “Three-Stage Model for Nucleation of Graphite in Grey Cast Iron,” Mater. Sci. Technol., **26**(12), pp. 1439–1447.

[12] 2020, “Taylor and Francis Online” [Online]. Available: https://www.tandfonline.com. [Accessed: 09-Nov-2020].

[13] Strande, K., Tiedje, N., and Chen, M., 2017, “A Contribution to the Understanding of the Combined Effect of Nitrogen and Boron in Grey Cast Iron,” Int. J. Met., **11**(1), pp. 61–70.

[14] Stefanescu, D. M., 2005, “Solidification and Modeling of Cast Iron — A Short History of the Defining Moments,” Mater. Sci. Eng. A, **413–414**(2005), pp. 322–

333.

[15] Stefanescu, D. M., 2009, *Science and Engineering of Casting Solidification*, Springer US, Ney York, NY.

[16] Jung, S., Ishikawa, T., Sekizuka, S., and Nakae, H., 2005, “Effects of Sulfur on Interfacial Energy between Fe-C Melt and Graphite,” J. Mater. Sci., **40**(9–10), pp. 2227–2231.

[17] Buhrig-Polackzek, A., and Santos, D., 988, “Solidification of Eutectic Alloys: Cast Iron,” ASM Handb., **15**, pp. 168–181.

[18] Morrogh, H., and Oldfield, W., 1959, “Solidification Of Grey Cast Iron,” Birmingham Metall. Soc.

[19] Velichko, A., Holzapfel, C., and Mücklich, F., 2007, “3D Characterization of Graphite Morphologies in Cast Iron,” Adv. Eng. Mater., **9**(1–2), pp. 39–45.

[20] Fraś, E., Górny, M., and López, H. F., 2007, “Eutectic Cell and Nodule Count in Grey and Nodular Cast Irons,” Mater. Sci. Technol., **23**(9), pp. 1109–1117.

[21] “Thermocouple Temperature Limits” [Online]. Available: https://reotemp.com/thermocouple-temperature-limits/.

[22] Ferro, P., Borsato, T., Bonollo, F., and Padovan, S., 2019, “A Solidification Time-Based Method for Rapid Evaluation of the Mechanical Properties of Grey Iron Castings,” Int. J. Met., **13**(4), pp. 845–852.

[23] Goodrich, G. M., 2006, “Introduction to Cast Irons,” ASM Handb., **15**, pp. 785–811.

[24] Stan, S., Chisamera, M., Riposan, I., and Barstow, M., 2012, “Application of Thermal Analysis to Monitor the Quality of Hypoeutectic Cast Irons during Solidification in Sand and Metal Moulds,” J. Therm. Anal. Calorim., **110**(3), pp. 1185–1192.

[25] Kurz, W.; Fisher, D. J., 1992, *Fundamentals of Solidification,* Trans Tech Publications, Aedermannsdorf, CH.